Design and Assessment of Subscale Flexible High Aspect Ratio Wings

Punsara D. B. Navaratna*, Alessandro Pontillo†, Djamel Rezgui‡, Mark H. Lowenberg§, Simon A. Neild¶ and Jonathan E. Cooper‖
University of Bristol, Bristol, BS8 1TR, United Kingdom

High aspect ratio wings have been the focus of several recent studies for efficiency improvements in modern aircraft. Many numerical studies can be found in literature with some experimental validations. The work presented here describes the design, manufacture, and the ground testing of three wings with a half-span of 0.85 m and full-span aspect ratio of 19 aimed for the future wind tunnel studies of nonlinear geometric effects on static and dynamic behaviour. Comparisons with a numerical model featuring geometric nonlinearity is made. The wing design approach used here is unique in the sense that the wings are designed simultaneously such that each will have a different level of flexibility, with other parameters such as mass distribution remaining constant. These wings will be used in future experiments aimed at investigating the effects of geometric nonlinearity and flexibility on the overall flight dynamics of an aircraft model on a multi-degree-of-freedom manoeuvre rig. The design considerations and interdependent constraints are discussed. The designed wings were manufactured and assembled to identical mass distributions and in good agreement with numerical models in terms of stiffness and frequency response. The design process, challenges, and learned lessons are presented.

I. Introduction

HIGH aspect ratio wings (HARW) are currently a major focus for advancements in aircraft design due to the decrease in induced drag and resulting improvements in fuel efficiency [1]. The consequence of a slender HARW is that it inevitably becomes a very flexible structure. Such flexibility will have effects on both the static and dynamic response of the aircraft, which in turn will impact its design while considering those effects. The notable static effects are caused by geometric nonlinearity, causing the wing to deflect and alter the equilibrium conditions; as the wing deflects due to aerodynamic loads, the local lift of the wing will have an inboard component as the loads act perpendicular to the beam reference line. The resulting change to internal loads will affect the design of aircraft wings as well as impact the sizing and performance evaluation of aircraft during the preliminary design stages [1, 2].

Geometric nonlinearity has been shown to also cause dynamic phenomena such as limit-cycle oscillation (LCO) in numerical studies found in literature [3–5]; LCOs exhibited by HARWs have been predicted at critical speeds below the linear flutter speed induced by a disturbance which can also lead to chaotic behaviour at higher speeds. Such behaviour will be critical for the design of HARWs to avoid catastrophic failure. These studies were performed using a geometrically nonlinear structural model coupled with an unsteady aerodynamic model with stall.

Patil and Hodges in Ref. [6] highlighted the various static and dynamic nonlinear effects using a geometrically exact numerical method. The importance of geometric nonlinearity modelled in the structure (large exact steady-state deflection), aerodynamics (3D effects on coefficient distribution), and fluid-structure interface (applying aerodynamic loads onto the structure in the exact orientations) were studied. Structural geometric nonlinearity showed minor changes on the static solution but large static deflections had a major effect on the whole aeroelastic system, creating significant changes to the edgewise bending and twisting structural frequencies, which reduced flutter speed. Aerodynamic geometrical nonlinearity showed insignificant effects; a large deflected wing can be assumed to be a planar wing with negligible effect. Ignoring 3D tip effects will only have a minor impact on accuracy as well for HARWs. Geometric

*Research Associate, Department of Aerospace Engineering, p.bannehekanavaratna@bristol.ac.uk.
†Research Associate, Department of Aerospace Engineering.
‡Senior Lecturer, Department of Aerospace Engineering.
§Professor of Flight Dynamics, Department of Aerospace Engineering, and AIAA Senior Member.
¶Professor in Nonlinear Structural Dynamics, Department of Mechanical Engineering.
‖Airbus RAEng Sir George White Professor of Aerospace Engineering, Department of Aerospace Engineering, and AIAA Fellow.

accuracy of the fluid-structure interface was shown to be critical: exact calculation of the local angle of attack as well as application of the aerodynamic loads perpendicular to the chord reference line and flow vector are necessary to accurately capture the aeroelastic response.

The dynamic response of the aircraft can also be significantly altered by strong coupling between the flexible modes of the wing and rigid body modes, such as shown by the numerical study done by Patil and Hodges in Ref. [7] for a high-altitude long-endurance aircraft. The study showed that the low frequency flexible modes in particular play the most significant role in affecting the short period and phugoid modes. The rigid body modes showed no impact on the predicted flutter speed and as such can be found efficiently with a cantilever wing model. The numerical study in Ref. [2] also found a decrease in flexible mode frequencies, with a small increase to rigid body mode frequencies as well as reduced damping for all modes at high aspect-ratios.

Experimental studies confirming geometric nonlinearity are present in literature. Tang and Dowell in Ref. [8, 9] validates aeroelastic static tip deflections of a horizontally mounted 0.45 m HARW with a NACA 0012 aerofoil as well as confirmed the presence of LCOs, which matches well with numerical predictions in terms of oscillation frequency and onset velocity for small angles of attack. The static deflection of the wing and wing loading were varied by changing the root incidence of the wing and with the use of tip weights. Hysteresis was also observed for the onset of the LCO, which depended on the direction of change in wind speed. Frequency sweep gust response tests were also performed on the same wing in a vertical configuration [10]. In these tests, the measure of nonlinearity used was the wing root incidence since the linearised aeroelastic model is not dependent on wing root incidence. A root incidence other than zero will cause the wing to deflect, creating geometric nonlinearity. The wing was tested at a root incidence of 0 deg and 2 deg. The static tip deflection for a wing root incidence of 2 deg was 30 mm (6.7% of semi-span). The wing tip edgewise response amplitude was less than 2 mm, the tip flapwise response amplitude was less than 8 mm (1.8% of semi-span), and the tip twist response amplitude was less than 9 deg. The experiments showed good correlation with the numerical model which showed a slight increase in twist mode frequency and negligible change in bending mode frequencies as geometric nonlinearity was introduced by increasing the root incidence from 0 deg to 2 deg. The increase in twist frequency contradicts the numerical predictions in Ref. [10] which concluded that geometric nonlinearity creates a significant decrease to twist frequency along with an increase to edgewise bending frequency. This discrepancy may be associated with the small magnitudes in the experimental gust response tests, as stated in Ref. [10], and needs to be investigated further.

The work done in Ref. [11] is a more recent example of aeroelastic wind tunnel testing of a 2.4 m HARW (half-span aspect ratio of 10) in a vertical configuration. It provides comprehensive sets of data for numerical model validation purposes. Another recent work is the wind tunnel experimental campaign in Ref. [12] on another 0.55 m vertical cantilever wing (half-span aspect ratio of 5.5) which achieved deflections of up to 50% of semi-span.

Wind tunnel experimentation of flexible HARWs including rigid body modes is limited in current literature. Ref. [13] has explored rigid body coupling with the use of a flexible wing root suspension support. The support structure allows for wing root translation in heave, made possible by a pair of flexible beams whose length can be changed to vary the stiffness. The study showed negligible change to flutter speed with the heave mode due to large separations in frequency. Gust response tests showed significant coupling between the wing root heave mode and multiple wing flapping modes at particular gust frequencies, however, excitation of the second natural frequency of the supporting beams worsened the correlation with theory. The amplitude of aeroelastic responses were also too small to draw conclusions on geometric nonlinear effects.

The GLAMOUR project aimed at the research and validation of gust load alleviation techniques using aeroservoelastic models uses a half-model (1:6 scale) floor mounting system capable of free motion in heave and pitch [14]. Since the wing is vertical, it becomes a challenge to trim the aircraft to simulate flight. In addition, the lift produced does not balance the weight distribution of the wing; true free flight equilibrium will therefore be different. The friction within the motion system also affects the free-aircraft response.

A full-span aeroservoelastic joined-wing concept aircraft model has been tested at the NASA Langley Transonic Dynamics Tunnel on a motion rig allowing for rigid body heave and pitch [15]. The tests conducted were used for control law verification, parameter identification, and for the demonstration of gust load alleviation. The aircraft model had a span of 3.66 m for sufficient internal space for control and model support system hardware. Experiments to study coupled rigid body and flexible modes of the unique joined-wing aircraft configuration have been performed successfully.

A more recent study done by Shi et al. in Ref. [16] focused on the body freedom flutter of a full-span flying wing aircraft model within a wind tunnel. The experiment uses a wire suspension system, giving the aircraft model freedom in pitch, yaw, and heave. The experimental results showed good agreement with theoretical predictions. The body

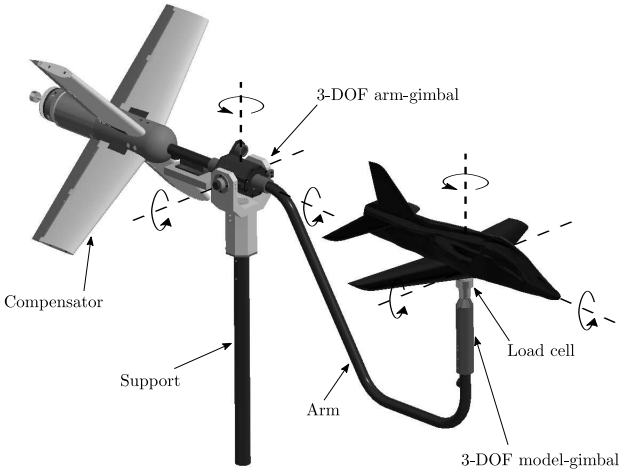

Fig. 1 The dynamic multi-DOF manoeuvre rig.

freedom flutter speed was found to be significantly affected by wing flexibility and lower to that predicted by a cantilever wing model.

Despite the previous studies, a full characterisation of the effects of geometric nonlinearity on the dynamic behaviour with experimental validation is limited in literature. In particular, the geometric effects on the overall flight dynamics and rigid body modes need further investigation. This paper considers a unique design case for subscale flexible HARWs for wind tunnel testing where three wings are designed simultaneously to have different levels of flexibility while keeping other properties such as mass distribution constant. This creates a unique challenge that has not been explored in literature before. The wings designed here will be used in future studies on an full-span aircraft model and flown on a multi-DOF manoeuvre rig to investigate the coupling between rigid body and flexible modes together with geometric nonlinear effects. Next the research aims of this paper and the overall project will be presented.

II. Research aims

The work presented in this paper is part of the EPSRC Flexi-Rig project testing campaign aimed at incorporating the multi-degree-of-freedom (multi-DOF) testing platform "manoeuvre rig" developed at the University of Bristol for low Reynolds number testing of flexible aircraft models. The rig has a total of five aircraft model DOFs: roll, pitch and yaw provided by a 3-DOF gimbal in the model, and approximate heave and sway provided by a pivoting arm attached to another 3-DOF gimbal, as seen in Figure 1. The rear of the rig has an aerodynamic compensator, which can be used to create forced rig motions or to attempt to compensate rig effects on the aircraft model response [17].

The manoeuvre rig has previously been used to study nonlinear and time-dependent aerodynamic effects such as LCOs and hysteresis in rigid body aircraft pitch, as well as for the development of mathematical models via parameter estimation and aerodynamic characterization of model aircraft [18–22].

Due to the DOFs available on the manoeuvre rig such as approximate vertical heave, the study of the effects of a flexible wing structure on overall flight dynamics can be made possible. In addition to longitudinal modes, lateral-directional asymmetric modes can also be studied on flexible aircraft models due to the available freedom of motion unique to the manoeuvre rig. However, the rig has its limitations: long period modes such as the phugoid cannot be replicated due to the inherent kinematic constraints present on the rig [17].

In the study presented in this paper, the design of three 0.85 m half-span cantilever wings with different flapwise bending stiffnesses are presented along with the challenges faced. The wings are unswept and non-tapered with a chord length of 8.95 cm, giving them a half-span aspect ratio of 8.94. The three flexibility cases are chosen to have a static trim tip deflection of 5%, 10% and 15% of the half-span. These wings will represent a fairly rigid wing, a moderately flexible wing, and a very flexible wing respectively. The ideal goal is to fix (or reduce the variation of) all other wing properties between these deflection cases, such as edgewise bending stiffness, torsional stiffness, and mass distribution. The unique challenges of meeting these specifications while meeting safety factor requirements, the design process, and decisions made are discussed in Section IV. The wings presented in this paper will continue onto an aircraft model with

a full-span aspect ratio of 19, and will be tested on the manoeuvre rig in future studies.

Wind tunnel testing will then be conducted on these half-span wings and will comprise static root incidence sweeps, followed by gust responses with the aim of characterising nonlinear geometric effects. The results will be compared with a geometrically nonlinear structural model coupled with a nonlinear unsteady aerodynamic model. Data acquisition consists of load measurements at the wing root and deflection responses measured non-intrusively by a camera system. These preliminary wind tunnel tests will provide valuable insight to gauge the capabilities and limitations of the manufacturing methods, precision, and accuracy of the designed wing properties.

III. Mathematical model

To help the design process of the wing a numerical model based on a low order geometrically exact "Nonlinear Beam Shapes" (NBS) structural model developed in Ref. [23] for highly flexible beams is used here. The reduced number of states is beneficial for fast computations during the optimisation process.

The coupled aerodynamic model incorporated within the NBS model is strip theory, with the spanwise distribution of coefficients obtained from the open source XFLR5 Vortex Lattice Method (VLM) [24]. In the work here, aerodynamic geometric nonlinearity is not considered; the spanwise aerodynamic influence coefficients (AICs) for a straight/planar wing are used. Ref. [6] concluded that assuming a planar wing to calculate local aerodynamics has little effect on the static or dynamic aeroelastic solution even for large deflections. The coefficient distribution takes into account tip effects. The geometrically-exact angle of attack used here as highlighted by Patil and Hodges [6] to be of major importance to capture aeroelastic characteristics. The applied aerodynamic loads are perpendicular to the wing reference line (1/4 chord here) and flow in order for the fluid-structure interface to be geometrically exact. Note that 3D drag estimated by XFLR5 is used here which, in addition to the inviscid drag calculated by VLM, also has a viscous component interpolated from the 2D viscous drag calculated by XFoil. A nonlinear unsteady aerodynamics model is currently being developed and will be coupled with the NBS structural model.

The structural model will also be compared with MSC Nastran's implicit nonlinear solution sequence (SOL 400). This is done by extracting the local aerodynamic loads in the exact orientations and applying them as follower forces and moments onto the equivalent Nastran finite element beam model.

IV. Subscale model wing design

A major aim of the project is to explore the effects of flexible HARWs on the overall flight dynamics of an aircraft model. To achieve this, an aircraft model capable of interchangeable wings having a range of flexibility will be tested on the 5-DOF manoeuvre rig. The aircraft model will be tested with three wings with the following general characteristics: a fairly rigid wing, a moderately flexible wing, and a highly flexible wing - designated according to their tip deflections (5%, 10% and 15% respectively), as previously stated. Note that here the total aircraft mass affects each case since the wing deflections are for trim equilibrium conditions; a heavier aircraft model fuselage requires a larger wing loading and therefore a stiffer wing to meet deflection requirements. Since the manoeuvre rig DOFs allow for aircraft model translation and rotations about all three axes, both mass and inertia need to be scaled in order to be representative a full-scale aircraft. A capability of the manoeuvre rig is that it can change the effective weight of the aircraft model using the rig's compensator to apply a constant force through the model's centre of gravity if located at the point of rotation.

The wings are non-swept and non-tapered with full-span of 1.7 m (half-span of 0.85 m) and chord length of 0.0895 m. The full span aspect ratio is 19 (half-span of 8.94). The tests will be conducted at a wind speed of 20-30 m/s. The Reynolds number is approximately 150,000. Figure 2 shows a drawing of the concept aircraft within the $7' \times 5'$ closed section wind tunnel.

Note that preliminary wind tunnel testing will be for the wings only (5%, 10%, and 15% tip deflection cases), mounted in a cantilevered manner in the tunnel. This section describes the aspects considered during the design of these wings and the decisions taken. The challenge with the design was mainly associated with the small volume available within the wing which caused difficulties with the manufacture of the spars to meet design criteria,

A. Segmented wing

The skin of the wings will consist of rigid 3D printed segments each attached by a single rib onto the beam at their centres. The material used for both the skins and ribs is PA-12 carbon-filled nylon due to its high strength and stiffness properties. The gaps between each rigid segments are not filled due to the unknown stiffness and damping effects it may have on the structural properties. By not filling the gaps, the rigid segments will have minimal impact on the stiffness

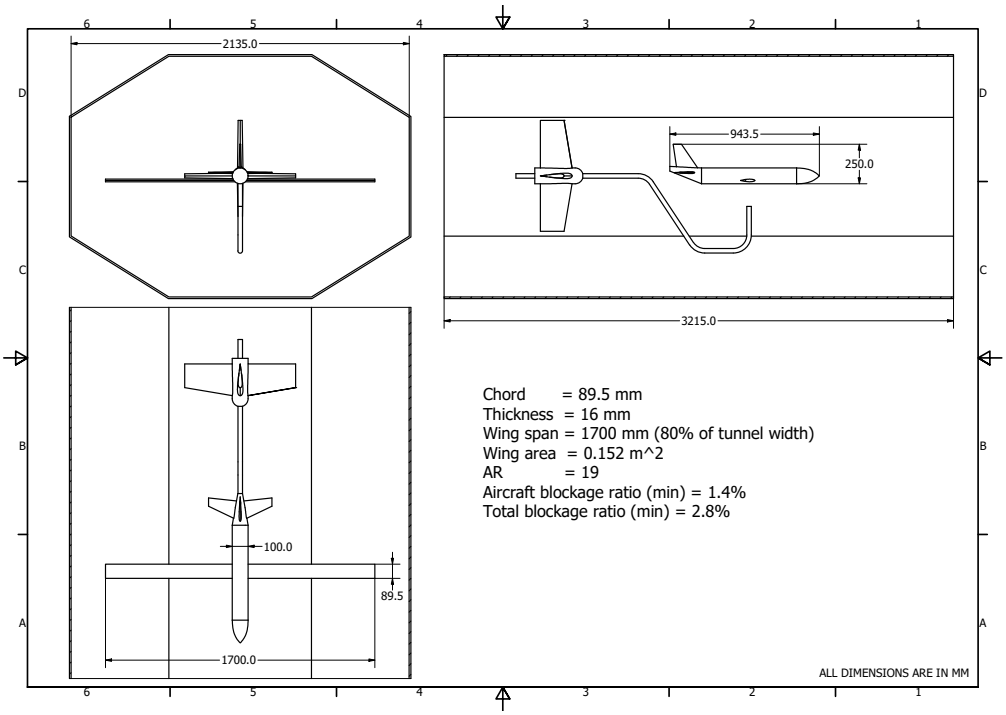

Fig. 2 General drawing of the concept HARW aircraft model and the manoeuvre rig.

and damping of the wing and focuses the design on the spar alone. The effects of filling the gaps on the aerodynamic loads (especially drag) as well as on the stiffness and damping characteristics are topics of interest in the project and will be looked at in a separate study. A gap width of 2 mm is chosen for all wing cases and determined by the largest deflection case.

The following is a list of effects on wing properties caused by a larger number of aerodynamic segments used:

1) Provides a smoother change in surface deflection, which is favourable.
2) A greater number of gaps between segments causing interference with the airflow, which is unfavourable.
3) An increase in wing mass due to the increased number of rib attachments required, which is unfavourable since the wing needs to be lightweight and resemble a flying model aircraft.

Figure 3 shows the effects on the half-wing root loading due to three, five, seven, and a 1000 wing segments (represented by case number respectively) found using the NBS method. Here the root pitch angle is trimmed such that a total vertical lift of 9.81 N is produced (1 kg per wing) at 20 m/s wind speed. Note that here the aerodynamic effects caused due to the gaps between segments are not considered. The percentage indicated under each data point is the difference relative to the 1000 wing segments reference (case 4). Figure 4 shows the changes in pitch, vertical tip deflection, and tip rotation for the same number of wing segment cases. Considering these effects, a total of five rigid segments per half-span was chosen as a suitable compromise. The largest difference to be expected would be in axial shear and will be less than 5% relative to a smoothly deflecting wing. The study conducted in Ref. [1] found that the largest effect on root loading due to geometric nonlinearity is expected to be on axial shear, in-plane shear, axial torque, and in-plane bending.

Figure 5 shows the CAD drawing of an iteration of a wing displaying the outer 3D printed skin (shown as semi-transparent parts) attached to the beam via 3D printed ribs. The same five outer printed surface segments will be attached onto each wing in order to reduce possible variations in results caused by differences in surface details and improve comparability.

With regards to the wing aerofoil section, the NACA0018 was chosen for the following reasons:

1) Since the scale of the model is small (half-span of 0.85 m and chord of 0.0895 m) the thickness of the wing needs to be adequate in order to contain the internal structure, attachment parts, and future control surfaces (which will be needed when the wings are combined with the fuselage and empennage to form the model to be tested on the manoeuvre rig).

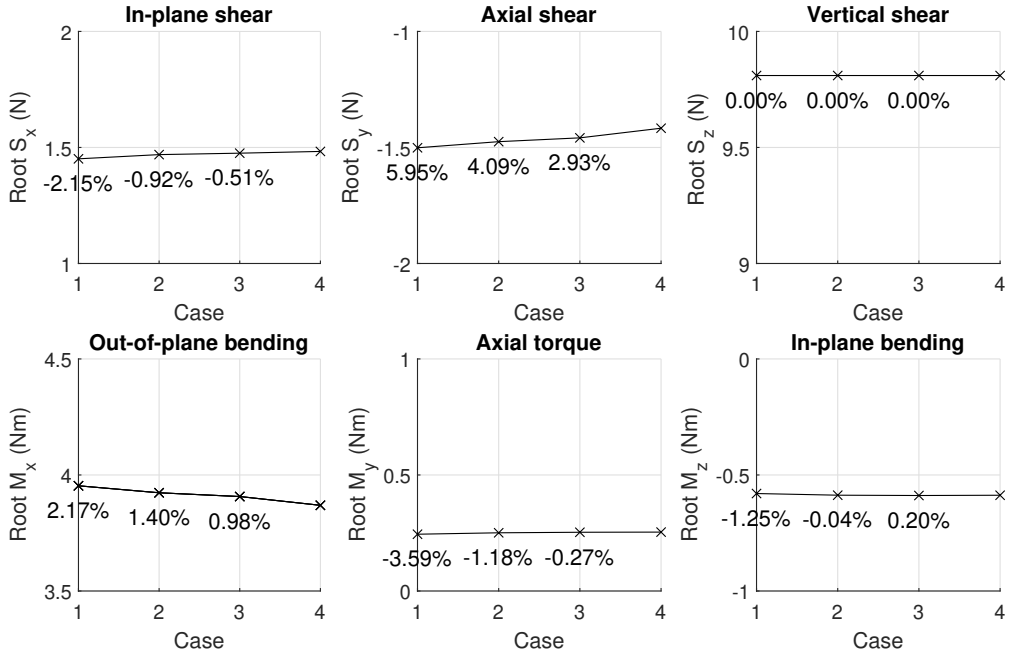

Fig. 3 Variations in wing root loading due to the number of rigid wing segments cases: 1) three segments, 2) five segments, 3) seven segments, and 4) 1000 segments.

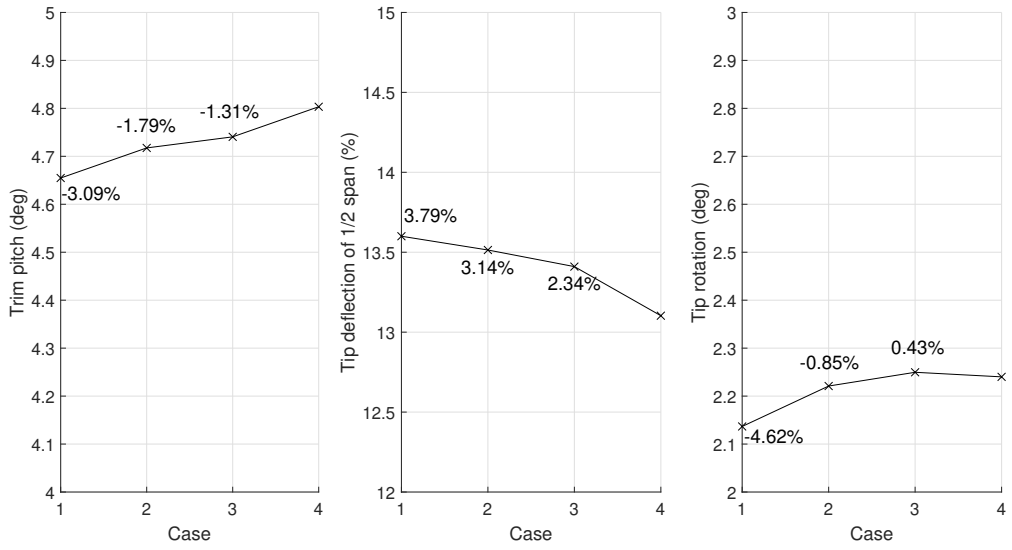

Fig. 4 Variations in trim root pitch angle, vertical tip deflection, and tip rotation due to the number of rigid wing segments cases: 1) three segments, 2) five segments, 3) seven segments, and 4) 1000 segments.

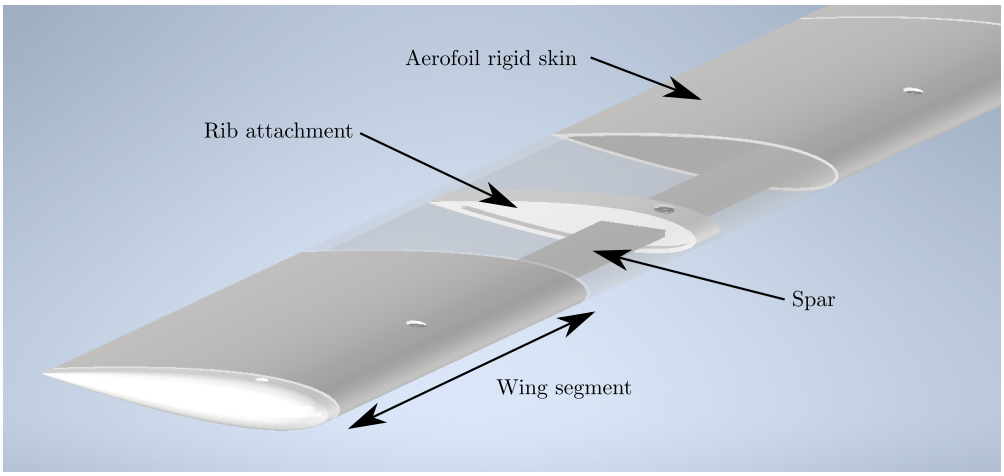

Fig. 5 CAD model of an iteration of a wing.

2) The chosen aerofoil has been shown to exhibit nonlinear dynamic phenomena such as stall flutter which can be observed and lead to interesting phenomena on HARWs [25, 26] and may provide interesting interactions with the flight dynamics modes.

B. Beam design and mass distribution

The load bearing structure of each wing is a single spar. Aluminium 7075-T6 was chosen as the material due to its high ratio between yield strength and elastic modulus, and can be machined well. The ideal case (and challenge) for each wing would be to vary only the flapping bending stiffness to achieve the required static aeroelastic deflection requirements while keeping every other structural property constant. The other wing structural properties considered here are edgewise bending stiffness, torsional stiffness, mass distribution, as well as the neutral and shear axes positions.

Similar to Ref. [27], the bending stiffness about both axes and torsional stiffness can be controlled by careful design of the beam cross-section. During initial stages of the design, two beam cross-sections were considered: a hollow rectangular section, and a U-section. Both these sections have sufficient number of dimensions that can be varied to satisfy flapping bending second moment of area, edge-wise bending second moment of area, and torsional constant simultaneously. It was found that the U-section has a larger range of possible property combinations compared to the hollow rectangular section. Figure 6 shows solution spaces for a non-tapered U-section beam with a constant torsional rigidity (GJ = 3 Nm^2) for a range of beam masses at flapwise bending rigidity (EI) values of 10.4 Nm^2, 5.2 Nm^2, and 3.5 Nm^2 which corresponds to the the bending stiffness required for a vertical tip deflection of 5%, 10%, and 15% of semi-span respectively. Each solution point was attempted using the "GlobalSearch" function within the Global Optimisation toolbox in Matlab. A black marker represents a solution does not exist, and a red marker means a solution exists. It can be seen that having a non-constant thickness (t1≠t2) allows for a beam with a lower mass of 0.15 kg. Figure 7 shows the same t1≠t2 study but for an increased torsional rigidity of GJ = 4 Nm^2 and GJ = 5 Nm^2. It can be seen that minimum mass increases for the GJ = 4 Nm^2 compared to the GJ = 3 Nm^2 case, and no solution exists for the 15% deflection case when GJ = 5 Nm^2.

However, due to the small scale of the model and manufacturing difficulties for a U-section, it was decided that the first iteration of the main spar will have a simple rectangular section. As a result, the edgewise bending stiffness and torsional stiffness are not controlled. To reduce the variation in edgewise bending and twist between wing cases, the difference in second moment of area ratio between edgewise and flapping axes will be large, and the spar is placed as close to the $1/4$ chord position as possible. Machining the beam to small thicknesses will prove difficult due to the possibility of distortion. The rectangular section spars will have a constant thickness as they are machined from aluminium 7075-T6 sheets. Another problem with a U-section is that the shear centre would not be colinear with the neutral axis, both of which are preferred to be placed at the aerofoil symmetry line for symmetric flapping deflections. A hollow rectangular section will have colinear shear and neutral axes, but is limited by available beams with set inner dimensions. More complex sections will be looked into for future wing iterations.

A static safety factor of two is used for the cantilever wings with the limit load case being 20 deg root incidence and

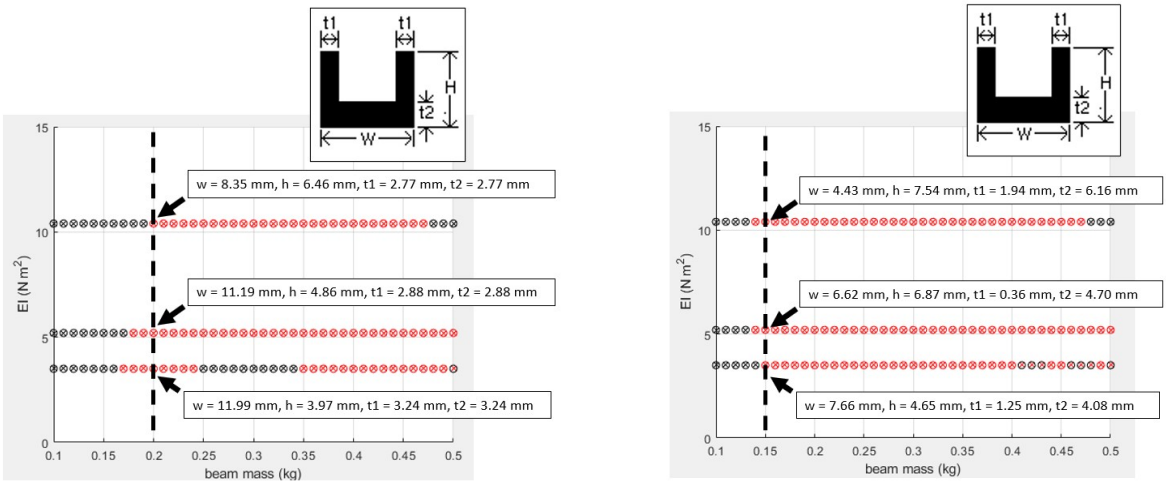

(a) **(b)**

Fig. 6 Solution space of a non-tapered U-section beam with a constant torsional rigidity of GJ = 3 Nm^2 for when (a) t1=t2, and (b) t1≠t2.

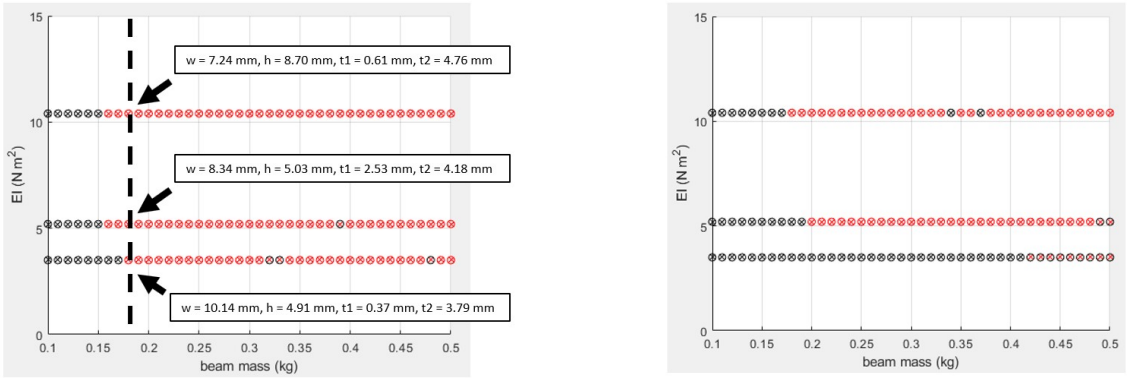

(a) **(b)**

Fig. 7 Solution space of a non-tapered U-section beam with torsional rigidity of (a) GJ = 4 Nm^2, and (b) GJ = 5 Nm^2.

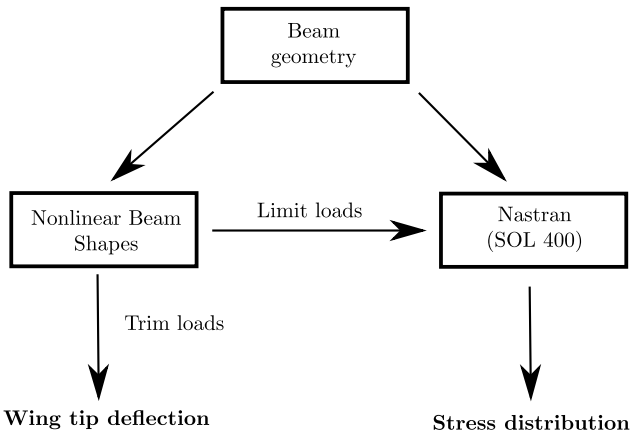

Fig. 8 Calculation of wing tip deflection and stress distribution.

30 m/s wind speed. Since the aerodynamic model used is linear and does not include stall, the design will be conservative and have an additional margin of safety. Dynamic load cases will be considered later with an unsteady nonlinear aerodynamic model. A non-tapered beam cannot meet the deflection and safety factor requirements simultaneously for the limit load case considered here. Therefore, the beam has to be tapered with a larger section at the root. The beam will have an inboard and outboard region where the cross-section will remain constant, and a region in between where the cross-section transitions from one to the other. The schematics of the beams are presented here following the description of the optimisation process.

Since the wings will be in the horizontal orientation when on the aircraft model, their mass distributions will have a significant effect on the aeroelastic response. The mass distribution needs to be kept constant between wing deflection cases. Since the beam dimensions are varied between cases to meet the deflection and safety factor requirements, the beams for each case will have a unique mass distribution. In order for the overall mass distribution to be constant between cases, additional masses are placed at each rib location. Each of the five half-span wing segments are considered as a single mass which will include the part of the spar within each respective segment. The target mass distribution is determined by the stiffest wing case which has the heaviest spar, i.e. the 5% deflection case. The additional masses and their center of gravity locations are recalculated for each design iteration for the overall wing mass to remain constant and is dependent on the dimensions of the beam.

The optimisation process is described next. The Matlab Genetic Algorithm (GA) within the Global Optimisation Toolbox was used here for the primary reason being that it allows for discrete changes in design parameters. To aid with machining, the minimum variation in dimensions was set to 1 mm for the section, and 10 mm for transition locations. This is made possible by using integer constraints withing the GA algorithm. A population size of 50 was used with reasonable parameter boundaries such that the solution converges within 30 generations. Figure 8 shows the calculations done for each individual within the generation. The NBS structural model coupled with the aerodynamic model is trimmed to generate vertical lift equal to the total weight of the aircraft model (at 30 m/s wind speed) from which the trim wing tip deflection is obtained. This is repeated for the same beam geometry at limit load conditions (30 m/s with a root incidence of 20 deg) to obtain the load distribution; this is applied onto an equivalent Nastran structural model as follower loads from which the beam stress is obtained. The minimisation function (f) for the GA is shown in Eq. 1. Here S is the safety factor, δ is the vertical tip deflection as a percentage of wing half-span, and the subscript $target$ represents target values for the respective parameters, i.e. $S_{target} = 2$ and $\delta_{target} = \{5\%, 10\%, 15\%\}$.

$$f = \begin{cases} |S - S_{target}| + |\delta - \delta_{target}|, & \text{if } S < S_{target}. \\ |\delta - \delta_{target}|, & \text{otherwise.} \end{cases} \tag{1}$$

Schematics of the optimised beams are shown in Fig. 9. All optimised beam trim deflections are within 0.01% of their respective targets. The 5% and 10% deflection case beams both have a constant thickness of 3.15 mm, and the 15% deflection case beam has a thickness of 2.30 mm. Figure 10 shows the safety factor distribution between deflection cases where the more flexible 10% and 15% cases are observed to be the critical cases. Figure 11 displays the static trim spanwise deflections and twist distribution for each case simulated using the NBS method and compared with Nastran's

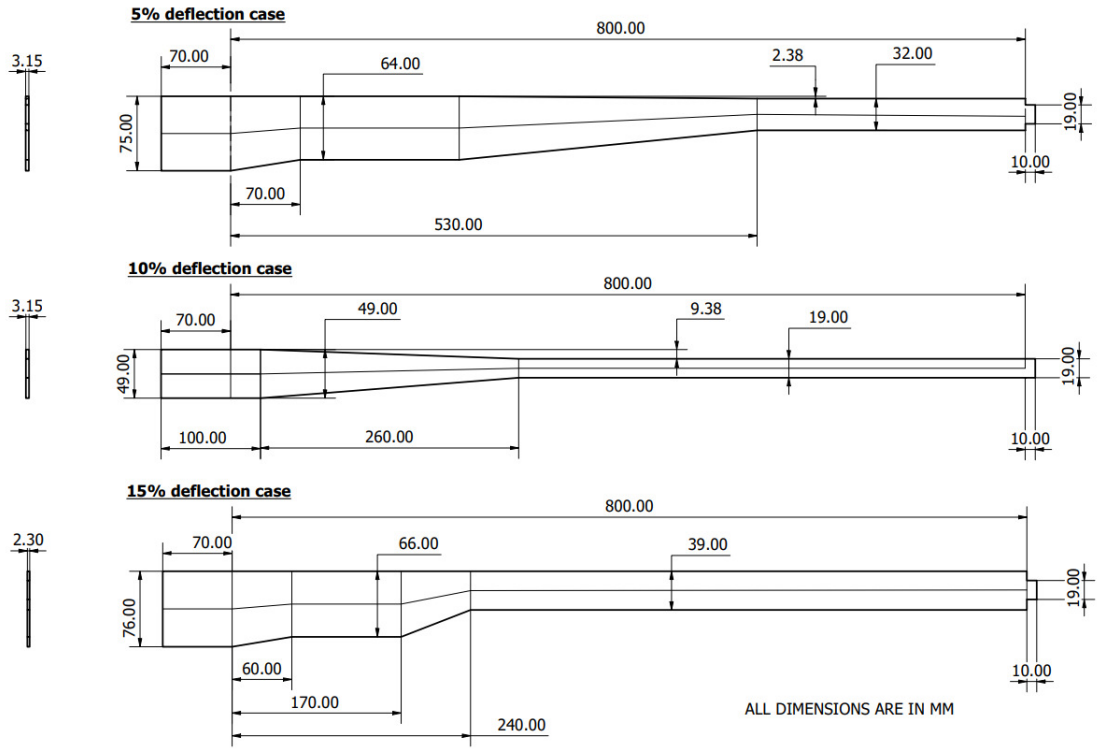

Fig. 9 Schematics of the optimised beams for each deflection case.

implicit nonlinear solutions, which shows a good match. The largest difference at the tip is 2.5% in vertical deflection and 5.6% in twist. The maximum twist for all cases is less than 0.6 deg.

Tables 1-3 show the target mass distribution required for each deflection case in order for each wing segment to have the same mass (within 1 gram) and centre of gravity location (within 1 mm) between test cases. The x-axis is chordwise (positive trailing edge to leading edge), y-axis is spanwise (positive root to tip), and z-axis is vertical (positive downwards). The origin is the wing root 1/4 chord position. The centre of gravity locations and mass moments of inertia (with respect to each center of gravity) are estimated using the CAD software Autodesk Inventor. Note that the mass moments of inertia were not parameters there were controlled during optimisation although they are of similar magnitudes between the test cases with the match being better for outboard wing segments especially in twist (about the spanwise y-axis). The additional mass for each segment consists of the wing skin, rib, screws, and brass parts glued onto each rib. Figure 12 shows the overview of each wing with all added masses. Each rib slides onto the spar and is tightened by a single grub screw at the trailing edge. No holes are made on the beams themselves to not compromise its strength. The skin then slides on top of the rib and is secured by two countersunk screws on the upper and lower surfaces which are offset in the chordwise direction to aid with alignment. The brass parts are cut from 2 mm brass sheets using Electrical Discharge Machining (EDM) and bent by hand to fit within the curved profile of the skin without contact with the beam.

V. Wing Assembly and Ground Testing

This section describes the assembly of all three wings followed by the static stiffness and vibration tests conducted. Comparisons with MSC Nastran's implicit nonlinear analysis (SOL 400) and normal modes analysis (SOL 103) will be made.

A. Wing assembly and mass distribution

First all three wings were assembled and their mass distributions were checked to make sure they match the target requirements described in the previous section.

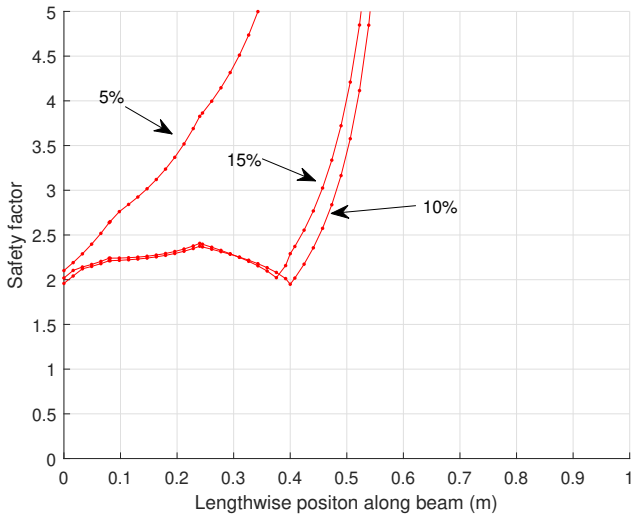

Fig. 10 Spanwise safety factor distribution for the optimised beams.

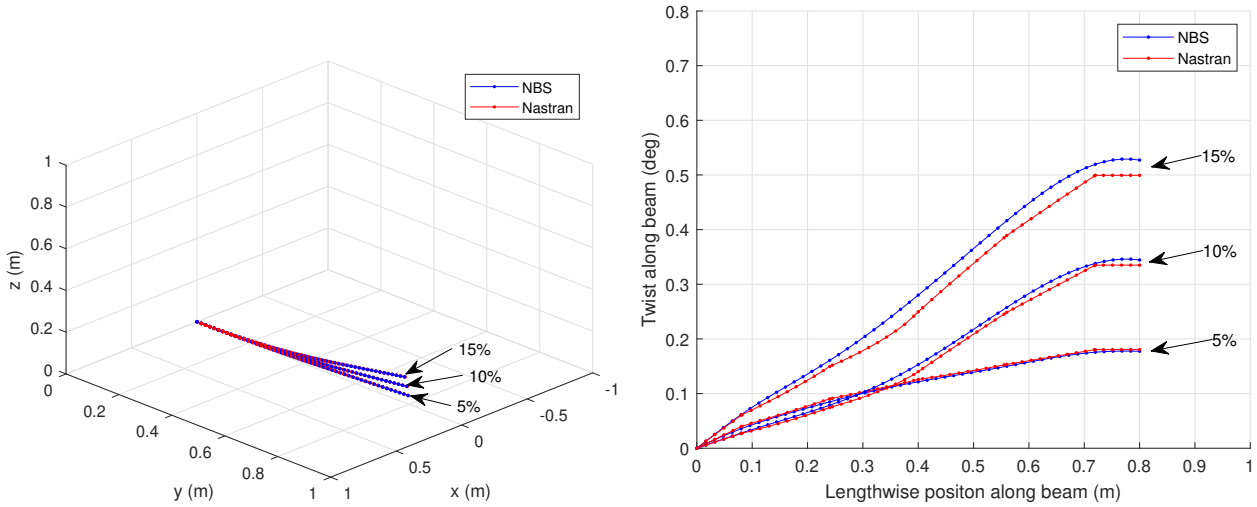

(a) **(b)**

Fig. 11 Comparison between NBS and Nastran structural models cases for static trim (a) deflections, and (b) twist.

Table 1 Target mass distribution for the 5% deflection wing

Segment	Beam mass (g)	Additional mass (g)	Total mass (g)	$x_{c.g.}$ (m)	$y_{c.g.}$ (m)	$z_{c.g.}$ (m)	I_{xx} (kg mm^2)	I_{yy} (kg mm^2)	I_{zz} (kg mm^2)
1	94.0	55.0	149.0	-0.016	0.079	0.000	307.1	81.3	369.6
2	87.0	45.0	132.0	-0.014	0.238	0.000	284.2	74.1	339.9
3	65.0	45.0	110.0	-0.011	0.398	0.000	238.3	59.7	281.3
4	46.0	52.0	98.0	-0.010	0.560	0.000	200.8	53.7	239.4
5	47.0	56.5	103.0	-0.010	0.725	0.000	246.8	54.4	287.6
Total	339.0	253.5	592.0						

Table 2 Target mass distribution for the 10% deflection wing

Segment	Beam mass (g)	Additional mass (g)	Total mass (g)	$x_{c.g.}$ (m)	$y_{c.g.}$ (m)	$z_{c.g.}$ (m)	I_{xx} (kg mm^2)	I_{yy} (kg mm^2)	I_{zz} (kg mm^2)
1	60.0	89.0	149.0	-0.017	0.079	0.000	245.3	85.2	306.2
2	35.0	97.0	132.0	-0.014	0.238	0.000	203.1	66.5	244.5
3	27.0	83.0	110.0	-0.011	0.398	0.000	174.3	59.3	210.4
4	27.0	71.0	98.0	-0.010	0.560	0.000	167.9	58.5	203.7
5	28.5	74.5	103.0	-0.010	0.725	0.000	217.8	58.6	255.2
Total	177.5	414.5	592.0						

Table 3 Target mass distribution for the 15% deflection wing

Segment	Beam mass (g)	Additional mass (g)	Total mass (g)	$x_{c.g.}$ (m)	$y_{c.g.}$ (m)	$z_{c.g.}$ (m)	I_{xx} (kg mm^2)	I_{yy} (kg mm^2)	I_{zz} (kg mm^2)
1	70.0	79.0	149.0	-0.017	0.079	0.000	262.5	76.0	319.0
2	48.0	84.0	132.0	-0.014	0.238	0.000	222.1	66.0	268.6
3	41.0	69.0	110.0	-0.011	0.398	0.000	193.2	59.3	233.4
4	40.0	58.0	98.0	-0.010	0.560	0.000	189.8	57.7	228.8
5	41.5	61.5	103.0	-0.010	0.725	0.000	238.5	58.2	279.4
Total	240.5	351.5	592.0						

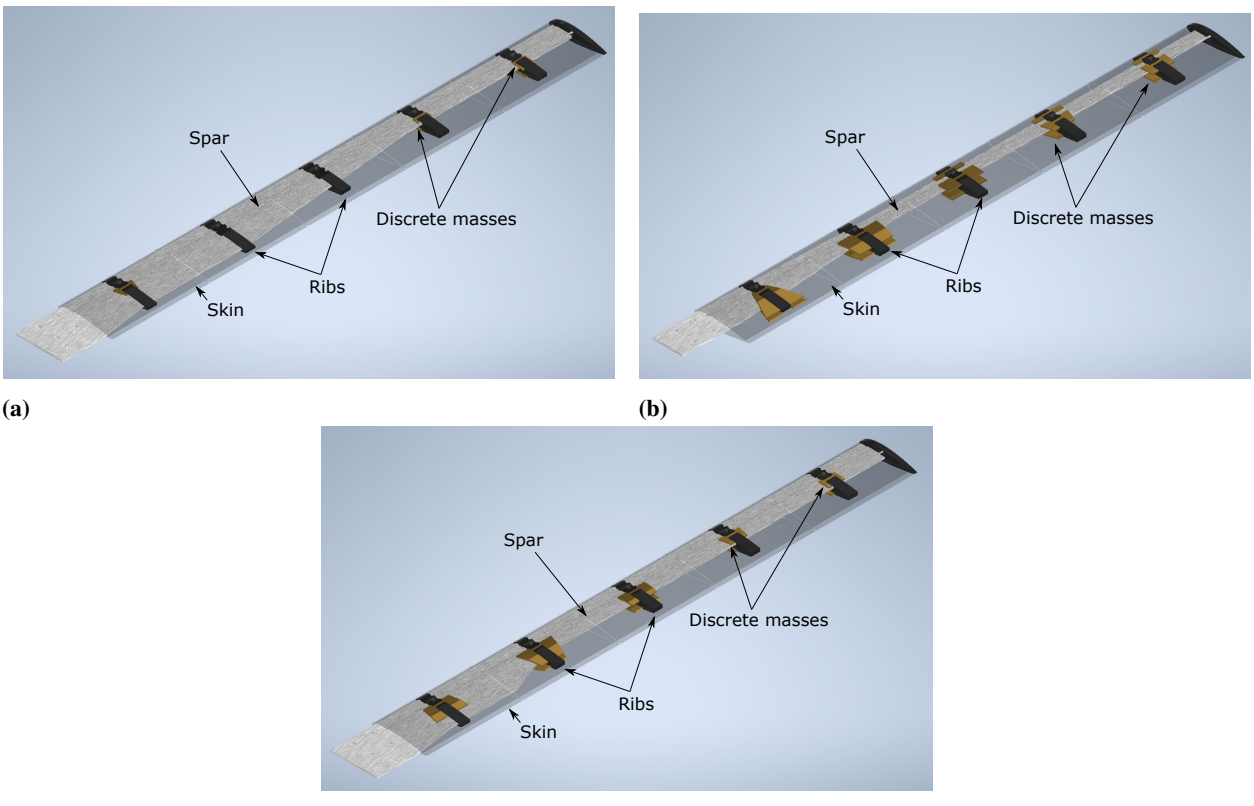

Fig. 12 CAD models for the (a) 5% deflection, (b) 10% deflection, and (c) 15% deflection case wings.

Table 4 Measured mass distribution for the 5% deflection wing

Segment	Beam (g)	Target		Measured		
		Additional mass (g)	Total mass (g)	Additional mass (g)	Total mass (g)	Total mass % difference
1	94.0	55.0	149.0	53.0	147.0	-1.3%
2	87.0	45.0	132.0	45.6	132.6	0.5%
3	65.0	45.0	110.0	47.5	112.5	2.3%
4	46.0	52.0	98.0	51.4	97.4	-0.6%
5	47.0	56.5	103.0	59.7	106.2	3.1%
Total	339.0	253.5	592.0	257.2	595.7	0.6%

Table 5 Measured mass distribution for the 10% deflection wing

Segment	Beam (g)	Target		Measured		
		Additional mass (g)	Total mass (g)	Additional mass (g)	Total mass (g)	Total mass % difference
1	60.0	89.0	149.0	87.0	147.0	-1.3%
2	35.0	97.0	132.0	97.6	132.6	0.5%
3	27.0	83.0	110.0	85.5	112.5	2.3%
4	27.0	71.0	98.0	70.4	97.4	-0.6%
5	28.5	74.5	103.0	77.7	106.2	3.1%
Total	177.5	414.5	592.0	418.2	595.7	0.6%

Tables 4-6 show the measured masses of each segment and the percentage difference with respect to the target. As stated before, the additional mass for each wing segment consists the skin, rib, screws, and brass masses. The largest differences in masses were caused by the 3D printed (PA12 carbon-filled) ribs and skin. The rib parts were consistently heavier by 1.0 g to 1.2 g than predicted, and the skin parts varies between being heavier by 0.5 g or lighter by 3.7 g than predicted. The reason for this mismatch could be due to the mass being dependant on the part geometry or inconsistent density. On the other hand, all the EDM cut brass parts were within ±0.1 g of their predicted mass. In order for wing segment masses to be consistent between test cases, additional mass was added in the form of epoxy which made the segment masses to be within ±0.05 g between test cases. The largest difference in segment mass is 3.1% (outer most segment) relative to the original mass target, with the overall wing mass being being 0.6% heavier than target. In hindsight, the variation in 3D printed part mass could have been taken into account by designing the brass parts after the 3D printed part masses were measured. The assembled wings can be seen in Figure 13.

Table 6 Measured mass distribution for the 15% deflection wing

Segment	Beam (g)	Target		Measured		
		Additional mass (g)	Total mass (g)	Additional mass (g)	Total mass (g)	Total mass % difference
1	70.0	79.0	149.0	77.0	147.0	-1.3%
2	48.0	84.0	132.0	84.6	132.6	0.5%
3	41.0	69.0	110.0	71.5	112.5	2.3%
4	40.0	58.0	98.0	57.4	97.4	-0.6%
5	41.5	61.5	103.0	64.7	106.2	3.1%
Total	240.5	351.5	592.0	355.2	595.7	0.6%

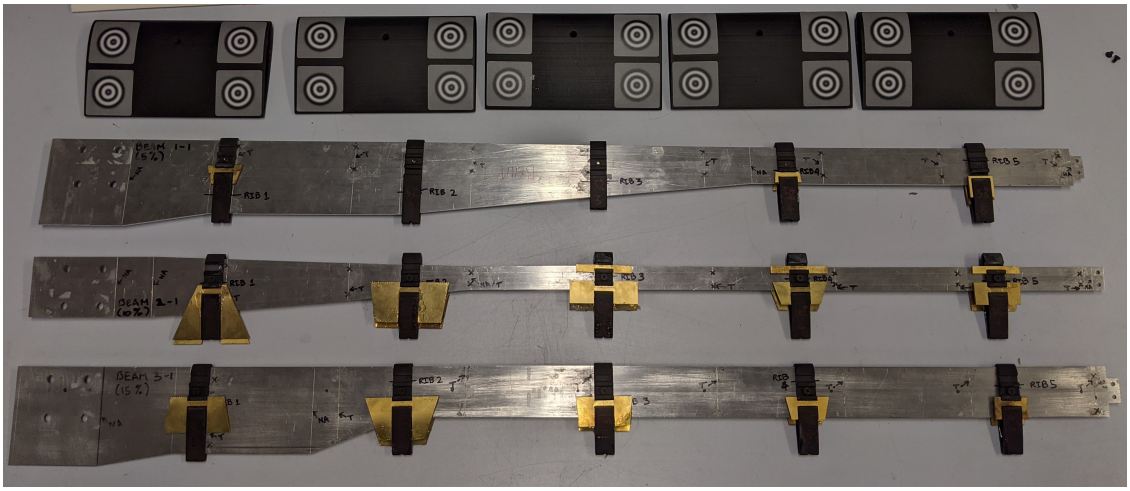

Fig. 13 Assembled wing spars with attached ribs and masses.

B. Static stiffness tests

The bending stiffness of each beam alone was confirmed by conducting static tip load tests. The beam deflections along the span were measured using an Imetrum stereo video gauge system capable of measuring translations remotely in three axes with a resolution of 1.3 μm to 11.0 μm. The system can measure up to a rate of 250 Hz and within a distance of 1.1 m to 2.1 m. The features used to track these displacements were bullseye markers placed on balsa wood paddles. The test setup is shown in Figure 14. Figure 15 shows the cantilever beam only deflection test for a range of tip masses. Note that ΔZ is the vertical displacement relative to the beam with zero tip mass. Downward deflections are positive. The measurements show good agreement with the nonlinear Nastran solutions where the largest difference found was 4.9% at the tip for the 15% beam test case for a tip mass of 88.0 grams.

Next the out-of-plane bending and torsional tests were performed on the fully assembled wings. This was done by applying a tip mass offset by 30 cm from the 1/4 chord position. The setup for this test can be seen in Figure 16. The displacement and twist for the outer most wing segment for a range of offset masses for all three test case wings are shown in Figure 17. Note that displacement (ΔZ) and twist ($\Delta\phi$) are relative to the wings with no tip mass. The trends in vertical displacement and twist show good agreement although some discrepancies are present in the displacement match for the 10% and 15% wings, and the twist for the 5% wing.

The in-plane bending stiffness was verified next using the same method as before but with the wing rotated by 87 degrees about the spanwise axis. The setup is shown in Figure 18. An angle of 3 degrees from the vertical plane was used to make the wing bend consistently in a single direction. Figure 19 shows the chordwise displacement for the outer most wing segment for a range of tip masses for all three test case wings. Again, good agreement with the Nastran analysis can be seen.

C. Vibration tests

Next, modal analysis is performed and comparisons to Nastran's Real Eigenvalue Analysis (SOL 103) are made. The test setup is shown in Figure 20. The wings are clamped onto the root structure in a 90 degree rotated orientation (about the spanwise axis) in order to avoid introducing nonlinearity caused by the curvature of the wings as it naturally deflects due to gravity. The wings are excited by a single shaker attached at the second wing segment rib location. The responses are measured using six accelerometers placed across the span of the wing. Two pairs of accelerometers are placed at the same span location but offset in the chordwise direction to capture torsional responses. The input signal generation and data processing is done using the Seimens LMS vibrations testing system. The included PolyMAX method is used to extract the mode frequencies, damping, and shapes [28]. The excitation signal used here is a burst random signal. The Nastran model includes the beam as 1D beam elements and all masses (including acclerometers) as lumped masses attached to the beam via rigid body elements. The interfaces between the ribs and spar are not modelled. The Lanczos method is used for computation, which is Nastran's recommended method.

Tables 7-9 shows the modal analysis results for all three test wing cases. Note that the frequencies in parenthesis for modes one and two are the mode frequencies obtained by Fast Fourier Transform (FFT) of displacement responses from

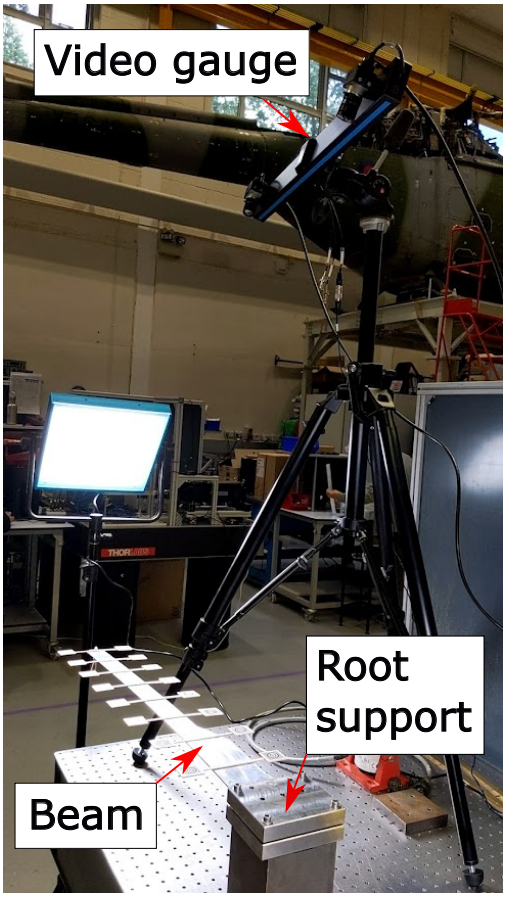

Fig. 14 Beam out-of-plane bending stiffness test.

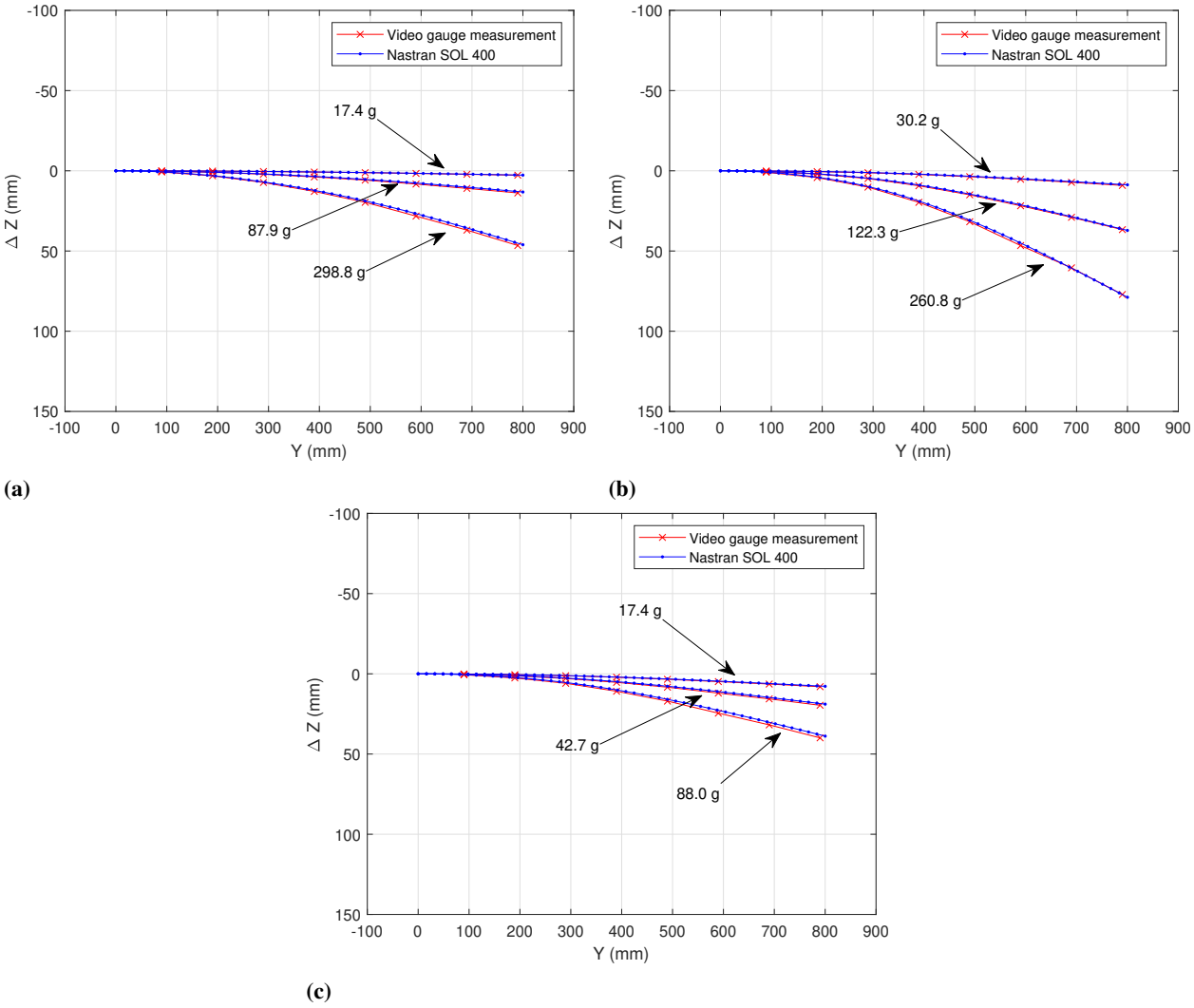

Fig. 15 Tip mass cantilever beam only out-of-plane bending stiffness comparison for the (a) 5%, (b) 10%, and (b) 15% test cases.

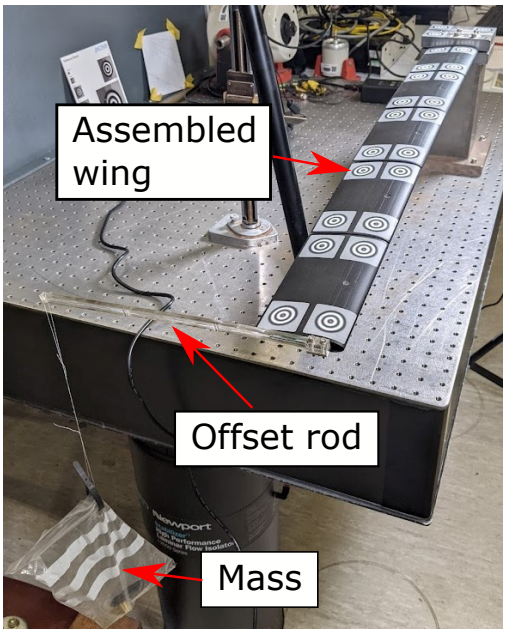

Fig. 16 Assembled wing out-of-plane bending and torsional stiffness test.

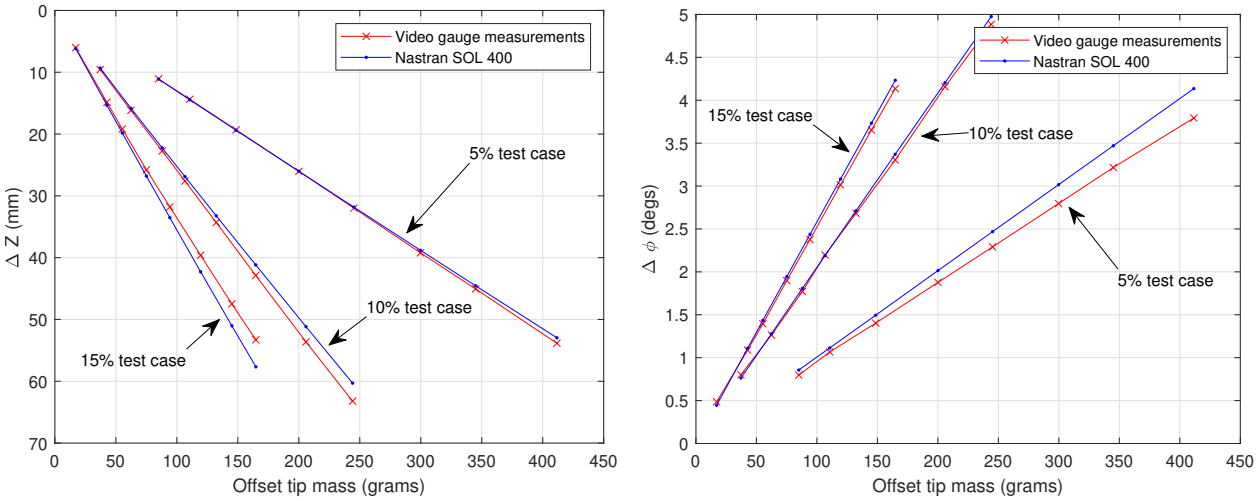

(a) **(b)**

Fig. 17 Offset tip mass cantilever wing out-of-plane bending and torsional stiffness test comparing (a) vertical displacement, (b) twist for the outer most wing segment.

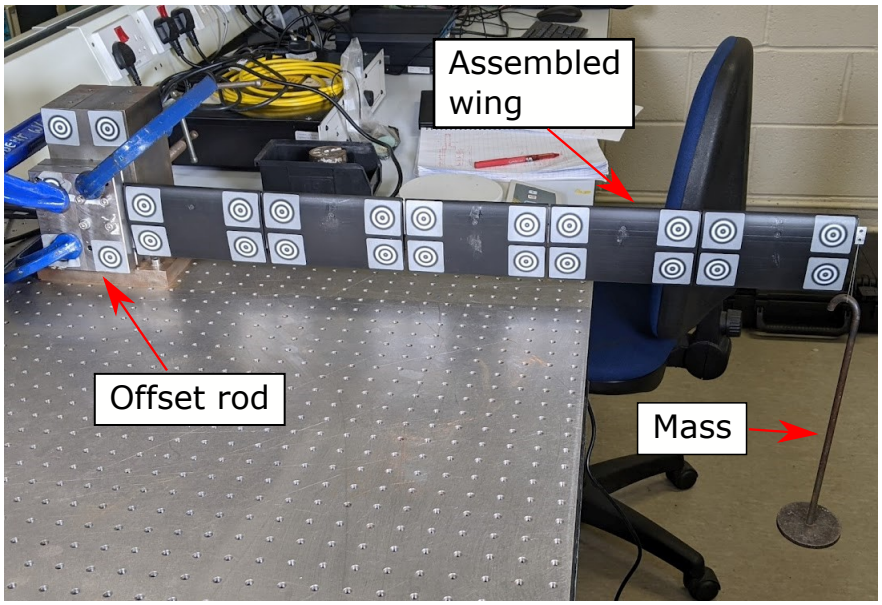

Fig. 18 Assembled wing in-plane bending stiffness test.

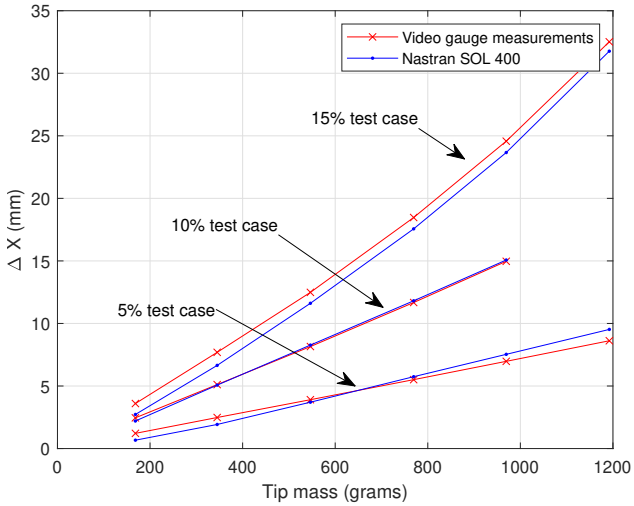

Fig. 19 Tip mass cantilever wing in-plane bending chordwise displacement for the outer most wing segment.

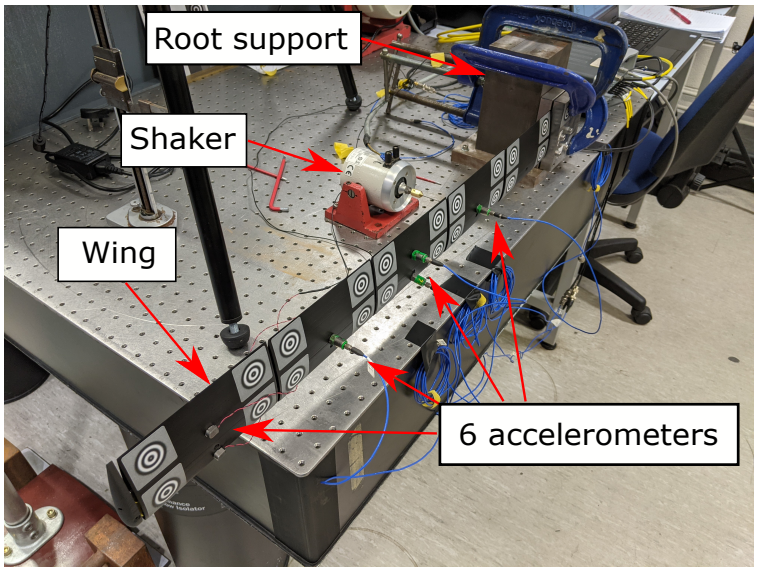

Fig. 20 Wing ground vibration testing setup.

Table 7 Modal analysis of the 5% deflection wing

Mode	Freq (Hz) Nastran	Freq (Hz) LMS	Damping LMS	Mode type
1	3.59	3.86 (3.59)	1.06%	Bending
2	18.91	18.32 (18.41)	0.44%	Bending
3	52.34	47.14	0.42%	Bending
4	61.31	61.79	1.48%	In-plane bending
5	101.99	86.01	0.81%	Bending
6	107.85			Torsion

the video gauge system at 250 Hz capture rate. This shows better agreement with Nastran predictions because the lowest frequencies are very close to the lower end of the accelerometer frequency bandwidth (1 Hz) which is likely causing errors. The measured frequencies match well with Nastran predictions especially for the lower frequency modes which are the main interest in the project since these will lead to strong coupling with rigid aircraft modes.

The gaps between the skin sections were chosen to focus the design efforts on the wing spars alone and to reduce stiffness and damping effects created by the skin thereby creating an overall lightly damped structure. However these gaps might have aerodynamic consequences such as vortex formation. The gap between the last wing segment and wing tip (which could affect the wing tip vortex) of the 15% test wing was covered by electrical tape (as shown in Figure 21) and a repeated vibration test showed an increase in damping of the first mode from 0.88% to 1.29%. The frequencies for all modes were unchanged.

Additionally, possible torsional coupling for limit cycle oscillation phenomena is of interest. The first torsional mode frequency for all wing cases is above 75 Hz. The effect of attaching additional mass at the wing tip trailing edge was looked into. Masses of 25.8 g and 52.0 g were attached and vibration tests repeated. The results are shown in Table 10. It can be seen that the frequencies for all modes are reduced significantly with the torsional mode frequency reduced by near identical amounts from 85 Hz to 53 Hz for both cases.

VI. Summary and conclusions

This paper considers a unique design study where three subscale flexible HARWs are designed simultaneously to have different levels of out-of-plane bending flexibility (5%, 10% and 15% tip deflection at design load) while other

Table 8 Modal analysis of the 10% deflection wing

Mode	Freq (Hz) Nastran	Freq (Hz) LMS	Damping LMS	Mode type
1	2.61	2.76 (2.58)	0.69%	Bending
2	13.79	13.42 (13.35)	0.41%	Bending
3	23.62	21.46	0.29%	In-plane bending
4	37.96	33.97	0.41%	Bending
5	71.73	62.92	0.34%	Bending
6	118.39	86.73	5.08%	Torsion

Table 9 Modal analysis of the 15% deflection wing

Mode	Freq (Hz) Nastran	Freq (Hz) LMS	Damping LMS	Mode type
1	2.14	2.48 (2.27)	0.88%	Bending
2	11.6	11.64 (11.67)	0.78%	Bending
3	27.98	28.63	0.43%	In-plane bending
4	32.14	41.36	1.18%	Bending
5	62.3	53.97	0.42%	Bending
6	77.1	85.09	1.10%	Torsion

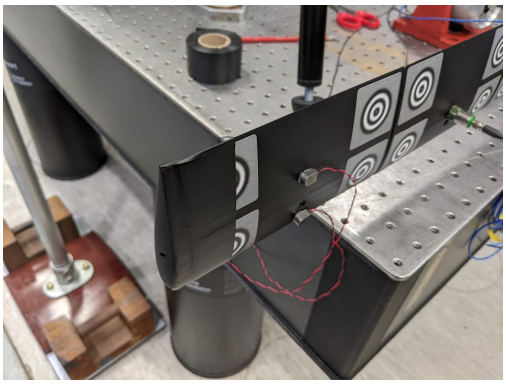

Fig. 21 Vibration testing of 15% wing with the tip gap covered with electrical tape.

Table 10 Modal analysis of the 15% deflection wing with added wing tip trailing edge mass

Mode	Tip mass = 0 g	Tip mass = 25.8 g		Tip mass = 52.0 g		Mode type
	Freq	Freq	% Diff	Freq	% Diff	
1	2.42	2.23	-7.82%	2.04	-15.74%	Bending
2	11.59	10.99	-5.20%	10.56	-8.84%	Bending
3	28.45	27.61	-2.95%	26.65	-6.32%	In-plane bending
4	41.15	34.67	-15.75%	32.04	-22.14%	Bending
5	53.87	41.34	-23.27%	38.28	-28.95%	Bending
6	85.08	53.23	-37.44%	52.98	-37.73%	Torsion

parameters are fixed. The design considerations and decisions taken to address this challenge were presented. The design and manufacturing process of three (0.85 m semi span) wings ranging from almost-rigid to highly flexible were described. Given the small wing section dimensions and available volume within the wing, meeting the required stiffness, safety factor, and mass distribution criteria simultaneously proved to be challenging. Furthermore,

Machining aluminium sections to small thicknesses was not possible due to distortion of the material. A genetic algorithm was used to solve the optimisation problem and three solutions were found. The load bearing structure is an aluminium 7075-T6 beam cut from a sheet with 3D printed ribs and skin made from PA12 carbon-filled material, which has high stiffness and strength nylon. The spars have a tapered rectangular cross-section (constant thickness). This means the edge-wise bending stiffness and torsional stiffness are not controlled. Their effects are reduced by having a relatively larger edge-wise bending section second moment of area (compared to flapping) and the spar being placed as close to the $1/4$ chord position as possible to reduce twisting caused by aerodynamic loads. The mass distribution was controlled by placing brass parts glued onto each rib. Although it was found that the 3D printed parts had varying density, it is possible to take the difference into account using the EDM cut brass parts with high accuracy. Gaps between skin segments were used to make the stiffness of the wing dependent on mainly the spar thus focusing the optimisation on it alone and aid predictability. In fact, modelling the spar alone was shown to be sufficient to capture the wing structural properties and the rib to spar interface had little effect. All three wings were made to have the the exact mass distribution with each having a total mass of 0.596 kg. Static stiffness tests of the wings conducted using a video gauge system measuring three axis displacements showed good agreement with the nonlinear numerical models capturing large deflections. Ground vibration tests of the wings using the PolyMAX method showed good agreement with Nastran's normal modes analysis for low frequency modes, which will be the focus of future studies exploring flexible wing coupling with rigid airframe modes. It is intended that the work presented in this paper will provide valuable insight into the challenges of designing and manufacturing of small scale highly flexible HARWs from the perspective of the unique design case considered here.

The next stage will be wind tunnel testing of the manufactured semi span wings to be compared with a geometrically nonlinear numerical model coupled with nonlinear unsteady aerodynamics. The wind tunnel testing will include:

1) Cantilever wing static wind tunnel tests for sweeps in wing root angle of attack.
2) Cantilever wing gust responses to sine and frequency sweep waves.

These wind tunnel tests will add to available literature for the validation of numerical models and the characterisation of nonlinear geometric effects on dynamic behaviour. The wings designed here will then be incorporated into a full subscale aircraft model to be tested experimentally on the manoeuvre rig to investigate rigid body coupling with flexible modes.

VII. Acknowledgments

The work presented in this paper is funded by the EPSRC funded Experimental Flight Dynamics Testing for Highly Flexible Aircraft project grant ref. EP/T018739/1.

References

[1] Calderon, D. E., Cooper, J. E., Lowenberg, M., Neild, S. A., and Coetzee, E. B., "Sizing High-Aspect-Ratio Wings with a Geometrically Nonlinear Beam Model," *Journal of Aircraft*, Vol. 56, No. 4, 2019, pp. 1455–1470. https://doi.org/10.2514/1.C035296.

[2] Cook, R. G., Calderon, D. E., Cooper, J. E., Lowenberg, M. H., and Neild, S. A., "Industrially Inspired Gust Loads Analysis of Various-Aspect-Ratio Wings Featuring Geometric Nonlinearity," *Journal of Aircraft*, Vol. 57, No. 1, 2020, pp. 13–28. https://doi.org/10.2514/1.C035294.

[3] Patil, M., Hodges, D., and Cesnik, C., *Limit cycle oscillations in high-aspect-ratio wings*, 1999. https://doi.org/10.2514/6.1999-1464.

[4] Tang, D., and Dowell, E., "Effects of geometric structural nonlinearity on flutter and limit cycle oscillations of high-aspect-ratio wings," *Journal of Fluids and Structures*, Vol. 19, 2004, pp. 291–306. https://doi.org/10.1016/j.jfluidstructs.2003.10.007.

[5] Modarres Aval, A., Bakhtiari-Nejad, F., Dowell, E., Peters, D., and Shahverdi, H., "A comparative study of nonlinear aeroelastic models for high aspect ratio wings," *Journal of Fluids and Structures*, Vol. 85, 2019, pp. 249–274. https://doi.org/10.1016/j.jfluidstructs.2019.01.003.

[6] Patil, M., and Hodges, D., *On the importance of aerodynamic and structural geometrical nonlinearities in aeroelastic behavior of high-aspect-ratio wings*, 2000. https://doi.org/10.2514/6.2000-1448.

[7] Patil, M. J., Hodges, D. H., and Cesnik, C. E. S., "Nonlinear Aeroelasticity and Flight Dynamics of High-Altitude Long-Endurance Aircraft," *Journal of Aircraft*, Vol. 38, No. 1, 2001, pp. 88–94. https://doi.org/10.2514/2.2738.

[8] Tang, D., and Dowell, E. H., "Experimental and Theoretical Study on Aeroelastic Response of High-Aspect-Ratio Wings," *AIAA Journal*, Vol. 39, No. 8, 2001, pp. 1430–1441. https://doi.org/10.2514/2.1484.

[9] Tang, D., and Dowell, E. H., "Limit-Cycle Hysteresis Response for a High-Aspect-Ratio Wing Model," *Journal of Aircraft*, Vol. 39, No. 5, 2002, pp. 885–888. https://doi.org/10.2514/2.3009.

[10] Tang, D., and Dowell, E. H., "Experimental and Theoretical Study of Gust Response for High-Aspect-Ratio Wing," *AIAA Journal*, Vol. 40, No. 3, 2002, pp. 419–429. https://doi.org/10.2514/2.1691.

[11] Cooper, J. E., Cook, R. G., Francois, G., Torre Rodríguez, Ó. d. l., Neild, S. A., Lowenberg, M. H., Alexander, S., Coetzee, E., and Evans, M., "Wind tunnel testing of a high aspect ratio wing model," *Proceedings of Forum of Aeroelasticity and Structural Dynamics IFASD 2019, 9-13 June 2019, Savannah, Georgia, USA*, Curran, 2019, pp. 094:1–094:26.

[12] Avin, O., Raveh, D. E., Drachinsky, A., Ben-Shmuel, Y., and Tur, M., *An Experimental Benchmark of a Very FlexibleWing*, 2021. https://doi.org/10.2514/6.2021-1709.

[13] Tang, D., Grasch, A., and Dowell, E. H., "Gust Response for Flexibly Suspended High-Aspect Ratio Wings," *AIAA Journal*, Vol. 48, No. 10, 2010, pp. 2430–2444. https://doi.org/10.2514/1.J050309.

[14] Ricci, S., Gaspari, A. D., Riccobene, L., and Fonte, F., *Design and Wind Tunnel Test Validation of Gust Load Alleviation Systems*, 2017. https://doi.org/10.2514/6.2017-1818.

[15] Scott, R., Castelluccio, M., Coulson, D., and Heeg, J., "Aeroservoelastic Wind-Tunnel Tests of a Free-Flying, Joined-Wing SensorCraft Model for Gust Load Alleviation," 2011. https://doi.org/10.2514/6.2011-1960.

[16] Shi, P., Liu, J., Gu, Y., Yang, Z., and Marzocca, P., "Full-Span Flying Wing Wind Tunnel Test: A Body Freedom Flutter Study," *Fluids*, Vol. 5, 2020, p. 34. https://doi.org/10.3390/fluids5010034.

[17] Banneheka Navaratna, P., Lowenberg, M., and Neild, S., "Minimally-constrained flight simulation in a wind tunnel," *Journal of Aircraft*, 2019. https://doi.org/10.2514/1.C035199.

[18] Araujo-Estrada, S. A., Lowenberg, M. H., Neild, S., and Goman, M., "Evaluation of Aircraft Model Upset Behaviour Using Wind Tunnel Manoeuvre Rig," *AIAA Atmospheric Flight Mechanics Conference*, 2015. https://doi.org/10.2514/6.2015-0750.

[19] Pattinson, J., Lowenberg, M., and Goman, M., "A multi-degree-of-freedom rig for the wind tunnel determination of dynamic data," *AIAA Atmospheric Flight Mechanics Conference*, 2009. https://doi.org/10.2514/6.2009-5727.

[20] Pattinson, J., Lowenberg, M., and Goman, M., "Characterisation of wind tunnel observed, large-amplitude pitch limit-cycles," *AIAA Atmospheric Flight Mechanics Conference*, 2011. https://doi.org/10.2514/6.2011-6526.

[21] Pattinson, J., Lowenberg, M. H., and Goman, M. G., "Multi-Degree-of-Freedom Wind-Tunnel Maneuver Rig for Dynamic Simulation and Aerodynamic Model Identification," *Journal of Aircraft*, Vol. 50, No. 2, 2013, pp. 551–566. https://doi.org/10.2514/1.C031924.

[22] Gong, Z., Araujo-Estrada, S., Lowenberg, M. H., Neild, S. A., and Goman, M. G., "Experimental Investigation of Aerodynamic Hysteresis Using a Five-Degree-of-Freedom Wind-Tunnel Maneuver Rig," *Journal of Aircraft*, Vol. 56, No. 3, 2019, pp. 1029–1039. https://doi.org/10.2514/1.C034995.

[23] Howcroft, C., Cook, R. G., Neild, S. A., Lowenberg, M. H., Cooper, J. E., and Coetzee, E. B., "On the geometrically exact low-order modelling of a flexible beam: formulation and numerical tests," *Proceedings of the Royal Society A: Mathematical, Physical and Engineering Sciences*, Vol. 474, No. 2216, 2018, p. 20180423. https://doi.org/10.1098/rspa.2018.0423.

[24] "XFLR5," http://www.xflr5.tech/xflr5.htm, 2021. Accessed: 2021-05-21.

[25] Fagley, C. P., Seidel, J., and McLaughlin, T. E., *Experimental Investigation of the Aeroelastic Behavior a NACA0018 Cyber-Physical FlexibleWing*, 2015. https://doi.org/10.2514/6.2015-2251.

[26] Fagley, C. P., Seidel, J., and McLaughlin, T. E., *Aeroelastic Response of a Finite Span NACA 0018 Wing Part 2: Computational Simulations*, 2015. https://doi.org/10.2514/6.2015-0250.

[27] Roskam, J., Holgate, T., and Shimizu, G., "Elastic wind-tunnel models for predicting longitudinal stability derivatives of elastic airplanes." *Journal of Aircraft*, Vol. 5, No. 6, 1968, pp. 543–550. https://doi.org/10.2514/3.43981.

[28] Peeters, B., Van der Auweraer, H., Guillaume, P., and Leuridan, J., "The PolyMAX Frequency-Domain Method: A New Standard for Modal Parameter Estimation?" *Shock and Vibration*, Vol. 11, 2004, pp. 395–409. https://doi.org/10.1155/2004/523692.